Polarity compensation mechanisms on the perovskite surface KTaO3(001)

Polarity compensation mechanisms on the perovskite surface $KTaO_3$ (001)

Authors: Martin Setvin,[1*] Michele Reticcioli,[2] Flora Poelzleitner,[1] Jan Hulva,[1] Michael Schmid,[1] Lynn A. Boatner,[3] Cesare Franchini,[2] Ulrike Diebold[1]

Affiliations:
[1] Institute of Applied Physics, TU Wien, Vienna, Austria
[2] University of Vienna, Faculty of Physics and Center for Computational Materials Science, Vienna, Austria
[3] Materials Science and Technology Division, Oak Ridge National Laboratory, Oak Ridge, Tennessee 37831, USA

*Correspondence to: setvin@iap.tuwien.ac.at

Abstract:

The stacking of alternating charged planes in ionic crystals creates a diverging electrostatic energy – a "polar catastrophe" – that must be compensated at the surface. We used scanning probe microscopies and density functional theory to study compensation mechanisms at the perovskite $KTaO_3$ (001) surface as increasing degrees of freedom were enabled. The as-cleaved surface in vacuum is frozen in place, but immediately responds with an insulator-to-metal transition and possibly ferroelectric lattice distortions. Annealing in vacuum allows the formation of isolated oxygen vacancies, followed by a complete rearrangement of the top layers into an ordered pattern of KO and TaO_2 stripes. The optimal solution is found after exposure to water vapor through the formation a hydroxylated overlayer with ideal geometry and charge.

One Sentence Summary:
All ionic materials have unstable, 'polar' surfaces and interfaces. We show how one system reacts in many different ways to alleviate the resulting energetic instability.

Main Text:

All ionic crystals can be considered as stacks of alternatingly charged lattice planes along certain crystallographic directions. When a crystal is terminated perpendicular to such a "polar" direction, the electrostatic energy diverges (*1,2*). The resulting instability can be compensated in various ways, e.g., by charge transfer, structural reconstructions, changes in the surface morphology, or by chemical doping (*3-5*). Such compensation mechanisms often create unusual physical and chemical materials properties (*6,7*).

Surface and interface polarity has been discussed controversially, particularly for perovskite oxides. These materials have a chemical formula ABO_3, where the larger A cation is 12 coordinate and the smaller B cation is 6 coordinate. Along the [001] direction, they contain AO and BO_2 planes that in many cases carry formal positive and negative charges. Tantalates and niobates (B=Ta or Nb) are prototypical examples of polar perovskites. Many exhibit (incipient) ferroelectricity (*8*), providing attractive options for electronics and sensors. The

built-in field can also enhance electron-hole separation in light-harvesting schemes (*9*); indeed, these materials are highly efficient photocatalysts (*10*) with a record quantum efficiency for photochemical water splitting >50% (*11*).

Because surfaces play a major role in all these applications, it is important to understand which response the system "selects" to relieve the electrostatic instability. We studied the polar (001) surface of $KTaO_3$ as a representative case using atomically-resolved microscopy and spectroscopy, integral surface analysis techniques, and density functional theory (DFT). We show that $KTaO_3$(001) undergoes an entire series of routes to polarity compensation.

A scanning tunneling microscopy (STM) image of the surface of a $KTaO_3$(001) single crystal after cleaved in ultrahigh vacuum (UHV) shows three steps running horizontally along the [100] direction (Fig. 1A). These steps have a height of ~0.4 nm, i.e., the $KTaO_3$ lattice constant. The entire area is covered by alternating KO and TaO_2 terraces separated by half-unit-cell steps. Interestingly, these terraces run uninterrupted across the full-height steps. The KO planes are always on top, while TaO_2 is in the ridge region (see the sketch in Fig. 1D); apparently the KO plane fractured more easily during cleavage. The KO and TaO_2 terminations have a formal charge of -1*e* and +1*e* per unit cell, respectively. The characteristic terrace size is 3 to 8 nm, and their ratio is 1:1. Thus, the top layer is polarity-compensated on a long-range scale (*2*).

Although the electronic structure appeared delocalized with no measurable atomic corrugation in STM, noncontact atomic force microscopy (nc-AFM) readily showed at atomic resolution a perfect (1×1) bulk-terminated structure with a low defect concentration. In a constant-height AFM image (Fig. 1B), the darker regions with atomic resolution correspond to the higher-lying KO terraces, and bright, uniform regions are lower-lying TaO_2 terraces. All of the AFM images were taken in constant-height mode, and on TaO_2 terraces the attractive forces were smaller because of the larger tip-surface distance. The AFM imaging mechanism on the KO terraces appears analogous to the prototypical NaCl(001) surface (*12*), which has an identical arrangement of surface ions. [Imaging the TaO_2 on the lower terraces proved more difficult, see Fig. S1 (*13*).]

Scanning tunneling spectroscopy (STS; Fig. 1C) showed that the two terminations had distinctly different electronic structures. The KO terraces had a wide band gap spanning from -3.5 to +1 V, whereas TaO_2 terraces appeared metallic (red/black curves in Fig. 1C) with a shallow state at -0.2 eV, and several deeper-lying states. These in-gap states did not appear on the smaller TaO_2 terraces (below ~8 unit cells size), and were also absent in the border area (~2 unit cell wide) around the KO islands (see the green spectrum in Fig. 1C). Figure 1E shows a representative spatial distribution of the in-gap states (more details are in Figs. S2, S3). These states exhibited a characteristic wave-like pattern with ~1.6 nm periodicity indicative of their delocalized (band-like) character (*14*). The derived wave vector is consistent with reported photoemission data (*15*).

The electric charge in the in-gap states counteracted the electrostatic potential arising from the TaO_2^+ polarity, but these states formed only when the terrace width (and related electrostatic potential) exceeded a certain critical limit. The situation bears similarities to the formation of the 2D electron gas at polar interfaces, where a critical film thickness is necessary (*6, 16*). These in-gap states already form on as-cleaved surfaces, which do not show any defects, and DFT calculations indicate a metallization of the surface (Figs. S4 and S5).

The uncompensated electrostatic potential is a driving force for further polarity-compensation mechanisms, and we estimated its magnitude using Kelvin probe force microscopy (KPFM; see Figs. 1F and S6). On as-cleaved surfaces, the local contact potential varied by ~0.3 V. Defect-free surfaces were only achieved for samples cleaved below room temperature. Annealing the surface in vacuum resulted in the development of more efficient polarity-compensation mechanisms. After raising the sample temperature to 312 K, defects

formed on the KO terraces (Fig. 2A,B). AFM images of these defects agreed well with Cl vacancies observed on the prototypical NaCl (001) surface (*12*) (see Fig. S7). Accordingly, we attributed the defects here to O vacancies, the corresponding formal charge of +2*e* being suitable for compensating the negative charge of the KO regions. The vacancies appeared in central regions of larger terraces, *i.e.,* at the locations with the highest electrostatic potential. The O vacancies were likely created by the migration of O atoms from the KO terraces toward the interface with TaO_2.

Annealing at higher temperature (T=387 K in Fig. 2C) resulted in small "holes" in the central regions of the KO terraces. The steps aligned more along <110>, the nonpolar step direction of KO (see the structural model in Fig. 2G). Upon further annealing to 482 and 517 K, the holes interconnected (Fig. 2, D and E, respectively), and formed a labyrinth-like structure. At the atomic scale, the surface still had the original bulk (1×1) termination, and KO and TaO_2 terraces alternated in a quasiperiodic pattern separated by half-unit steps. The ratio of KO:TaO_2 remained 1:1, indicating that the process is only caused by KO rearrangement without desorption or diffusion from or to the bulk. KPFM measurements (Fig. S6) showed that the O-vacancy formation reduced the original electrostatic potential by half, and after the surface rearranged into the labyrinth structure, the measured potential variations were negligible.

The labyrinth structures had a characteristic terrace width of ~1.5 nm (4 to 5 atoms), that did not change upon further annealing. The pattern was remarkably stable up to 700 K. At even higher temperatures, the ordering was lost (Fig. S8), likely because of K segregation from the bulk (*17*). The 'magic' size of the stripes in Figs. 2, D to F, likely originated from a competition between two driving forces: Minimizing the terrace size suppressed the electrostatic potential arising from the polarity, while steps cost energy. This hypothesis was tested by calculating the surface energy and electrostatic potential as a function of terrace width. The structural model consisted of alternating KO and TaO_2 terraces of equal widths w (where w equals the number of K atoms in the 2D unit cell) separated by steps running in the [110] direction (Fig. 2G). The energy minimum was achieved for a w of 4 to 5 atoms (red curve in Fig. 2H), in agreement with the experiment. The electrostatic potential changed smoothly in the range $1<w<8$ and then started to deviate rapidly for higher w, indicating increasing polar instability.

Considering these calculations, the exact polarity-compensation mechanism of the as-cleaved KO terraces remains an open question. The low defect density and the absence of an electronic reconstruction should result in a relatively high electrostatic potential (>1 V), yet the experimental KPFM data (Fig. 1F and S6) showed considerably smaller potential corrugations. The incipient-ferroelectric character of the material could contribute to the polarity compensation, allowing for generation of electric fields inside the material at no energy cost. Our experimental indications are indirect, but the calculations showed ferroelectric-like lattice distortions (Fig. S9). Further, the sample cleaving always resulted in a very characteristic layout of the KO/TaO_2 terraces that crossed full steps without interruption (Fig. 1A). Strain-induced (*18*) spinodal decomposition into ferroelectric domains could occur during the cleavage, and the resulting terrace layout would be a "printout" of these domains (Fig. S9).

The most efficient polarity-compensation mechanism developed after exposing the surface to H_2O vapor (Fig. 3). Water induced a complete restructuring of the surface layer, even in UHV and at room temperature. After dosing 300 Langmuir (L) of water vapor at 325 K the surface was flat and had only full-unit-cell steps (Fig. 3A). More detailed AFM (Fig. 3B) showed a homogenous phase with a (2×1) symmetry; low-energy electron diffraction (Fig. S10) confirmed that the entire surface had been transformed.

This transition required high doses of water; Fig. 3C shows a surface exposed to 100 L H_2O. Here the occasional small island of the original bulk-terminated KO was found, interfaced

with the (2×1) overlayer. The (2×1) termination could be switched back to the (1×1), see Fig. 3D. Annealing above ~488 K in UHV resulted in water desorption, and formation of the same labyrinth-like structure of alternating KO/TaO_2 terraces as shown in Fig. 2, confirming reversibility between these two surface phases.

To determine the chemical composition of the (2×1) superstructure, low-energy He^+ ion scattering is an ideal method because it is only sensitive to the very top layer of the surface. The red curve in Fig. 3E was measured on an as-cleaved surface. As expected, O, K, and Ta are present. After dosing with water, the Ta signal completely disappeared (blue curve). X-ray photoelectron spectroscopy (Fig. S11) revealed the hydroxylated character of the (2×1) termination, and also excluded any possible contamination from the water exposure. It appears that water dissolved the KO islands and redistributed them across the TaO_2 planes. A proposed structural model is shown in Fig. 3F. Each KO unit reacted with one H_2O molecule, resulting in one $K(OH)_2$ unit per (2×1) unit cell. This termination was also polarity-compensated, with a net charge of -0.5*e* per (1×1) unit cell (*2*). A (2×1) termination of $KTaO_3$(001) has already been reported (*19*) and investigated theoretically (*20*), but the presence of water had not been considered.

The $KTaO_3$ (001) surface exhibited a rich spectrum of mechanisms for compensating the surface polarity, and a proper control of the environment can be used to tailor which one is at work. The phenomena observed on the as-cleaved surfaces, i.e., electronic reconstruction and ferroelectric lattice distortions, are well known from perovskite heterostructures. We could directly probe the character of the two-dimensional electron gas (2DEG)-like states and their spatial confinement to the highly polar regions. The labyrinth-like pattern formed upon annealing represents an interesting template for charge-carrier separation in light-harvesting devices, but protection against environmental influences would need to be facilitated for practical use. Although such a structure minimizes the surface energy, the corresponding energy gain is almost an order of magnitude lower compared to chemically-induced polarity compensation by water. The phase diagram in Fig. 3G shows that the mechanisms encountered in UHV decreased the surface energy by tenths of electron volts, whereas hydroxylation brought an order of magnitude higher energy gain. Perovskite surfaces in ambient conditions are typically hydroxylated and near the bulk-termination, but little is known about the exact surface structure. The (2×1) reconstruction observed here could therefore serve as a working model for future studies into the surface chemistry of perovskite oxides.

References and Notes:

1. P. W. Tasker. *J. Phys. C* **12**, 4977-4984 (1979).
2. C. Noguera. *J. Phys. Cond. Mat.* **12**, R367-R410 (2000).
3. A. F. Santander-Syro *et al. Nature* **469**, 189-193 (2011).
4. B. Meyer. *Phys. Rev. B* **69**, 045416 (2004).
5. O. Dulub, U. Diebold, G. Kresse. *Phys. Rev. Lett.* **90**, 016102 (2003).
6. S. Thiel *et al. Science* **313**, 1942-1945 (2006).
7. A. Bruix *et al. Angew. Chem. Int. Ed.* **53**, 10525-10530 (2014).
8. D. J. Singh. *Phys. Rev. B* **53**, 176-180 (1996).
9. I. Grinberg *et al. Nature* **503**, 509-512 (2013).
10. E. Grabowska. *Appl. Cat. B: Environmental* **186**, 97-126 (2016).
11. H. Kato, K. Asakura, A. Kudo. *J. Am. Chem. Soc.* **125**, 3082-3089 (2003).
12. L. Gross *et al. Phys. Rev. B* **90**, 155455 (2014).
13. *Supplementary Material available online*
14. M. Setvin *et al. Phys. Rev. Lett.* **113**, 086402 (2014).
15. P. D. C. King *et al. Phys. Rev. Lett.* **108**, 117602 (2012).

16. P. R. Willmott *et al. phys. Rev. Lett.* **99**, 155502 (2007).
17. K. Szot *et al. J. Phys. Cond. Matt.* **12**, 4687-4697 (2000).
18. J. H. Haeni *et al. Nature* **430**, 758-761 (2004).
19. T. W. Trelenberg *et al. J. Phys. Cond. Mat.* **22**, 304009 (2010).
20. D. Deacon-Smith *et al. Adv. Mat.* **26**, 7252-7256 (2014).
21. M. Prietsch, A. Samsavar, R. Ludeke. *Physical Review B* **43**, 11850 (1991).
22. G. Kresse, J. Furthmuller. *Computational Materials Science* **6**, 15-50 (1996).
23. J. P. Perdew, K. Burke, M. Ernzerhof. *Phys. Rev. Lett.* **77**, 3865-3868 (1996).
24. P. Zhang, J. Zhang, J. Gong. *Chem. Soc. Rev.* **43**, 4395-4422 (2014).
25. I. G. Austin, N. F. Mott. *Adv. Phys.* **50**, 757-812 (2001).
26. R. Bechstein *et al. Nanotechnology* **20**, 505703 (2009).
27. T. Y. Chien, J. Chakhalian, J. W. Freeland, N. P. Guisinger. *Advanced Functional Materials* **23**, 2565-2575 (2013).

Acknowledgments: The work was supported by European Research Council (ERC) advanced grant "Oxide Surfaces" (ERC-2011-ADG-20110209), Austrian Science Fund (FWF) Project Wittgenstein Prize (Z 250), Project F45 (FOXSI) and the FWF-SFB project VICOM (Grant no. F41). Research at the Oak Ridge National Laboratory for one author (LAB) was supported by the U.S. Department of Energy, Office of Science, Basic Energy Sciences, Materials Sciences and Engineering Division. All data are reported in the main text and supplement.

Supplementary Materials:

Materials and Methods

Figures S1-S11

References (21-27)

Coordinates Labyrinth-w5.cif

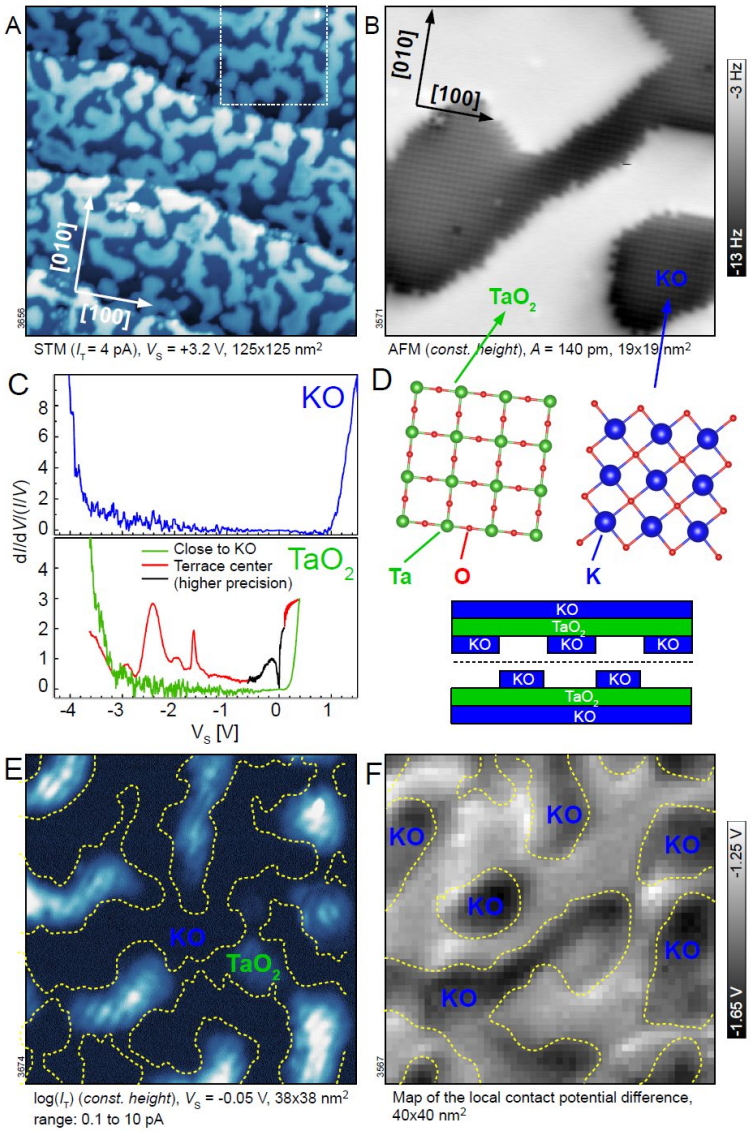

Fig. 1: Cleaved $KTaO_3$ (001). (A) Overview STM image of a surface prepared by cleaving at T=261 K. **(B)** Atomically-resolved AFM image. **(C)** STS spectra measured above the KO and TaO_2 terraces. **(D)** Atomic structure of the TaO_2 and KO terraces, and a schematic drawing of the cleaving. **(E)** Spatial distribution of in-gap states, measured in the region marked by a dashed square in **(A)**. Dashed lines mark steps. **(F)** Kelvin probe force microscopy image of a different region, showing the local electrostatic surface potential.

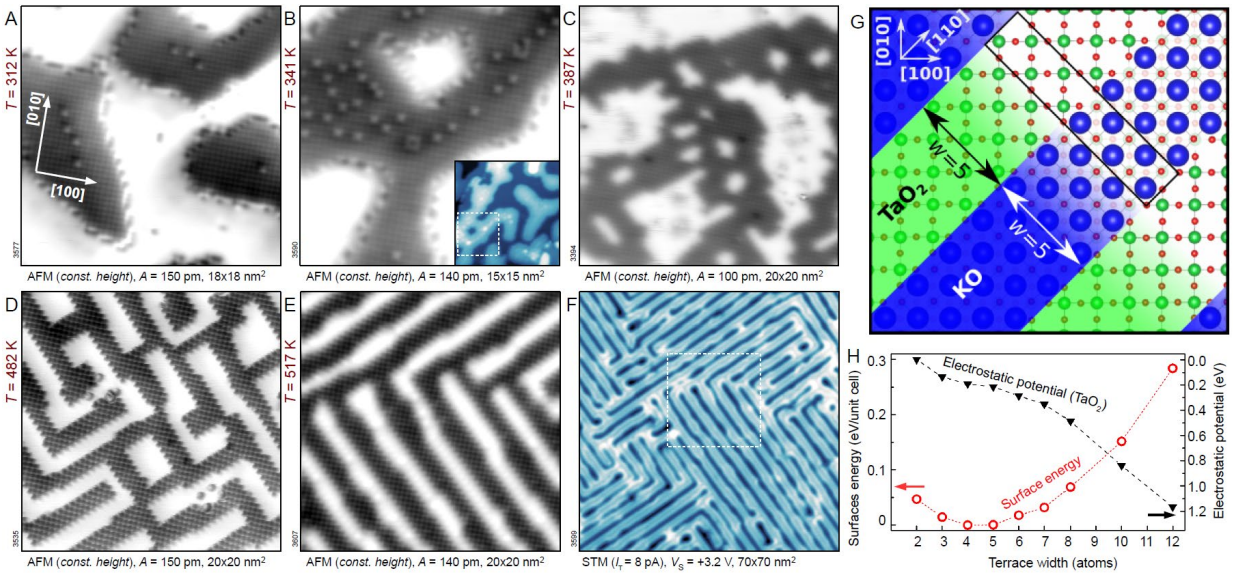

Fig. 2: Progression of surface structure with increasing annealing temperature. (A to E) AFM images of the surface after annealing in vacuum to 312, 341, 387, 482, and 517 K, respectively (measured at 4.8 K). The inset in **B** shows a larger-area STM image of the region. **(F)** Overview STM image of the surface shown in **E**; the corresponding area is marked by a dashed square. **(G)** Top view of the model used for the DFT calculations. The unit cell is marked by a rectangle. **(H)** Calculated surface energy and electrostatic potential in the center of the TaO_2 terrace as functions of the terrace width.

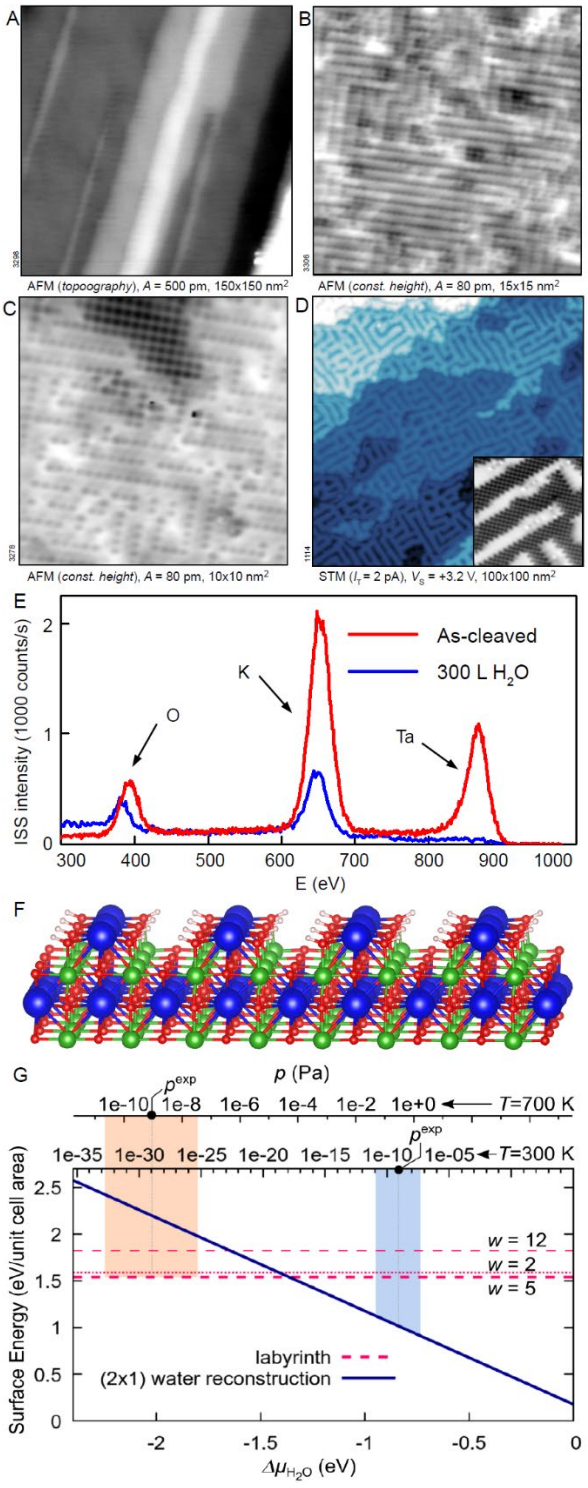

Fig. 3: Water-induced, hydroxylated (2×1) surface layer. (A) Overview AFM image of the $KTaO_3$ (001) surface after exposure to 300 Langmuir (L) H_2O at T=325 K. **(B)** Atomically resolved detail, showing a homogeneous superstructure with (2×1) ordering. **(C)** Surface exposed to 100 L H_2O at T=298 K, showing the interface between an original (1×1) KO terrace and the (2×1) phase. **(D)** The (2×1) surface after annealing to 488 K (inset shows an atomically resolved AFM image). **(E)** Low energy He^+ ion scattering spectra of the as-cleaved, bulk-terminated surface and the (2×1) overlayer. **(F)** Atomic model of the (2×1) overlayer. **(G)** Phase diagram for the transition between the (1×1) bulk-termination and the (2×1) structure.